

Improving Light Absorption in a Perovskite/Si Tandem Solar Cell via Light Scattering and UV-Down Shifting by a Mixture of SiO_2 Nanoparticles and Phosphors

Seongha Lee, Chan Ul Kim, Sumin Bae, Yulin Liu, Young Im Noh, Ziyu Zhou,
 Paul W Leu, Kyoung Jin Choi,* and Jung-Kun Lee*

The optical properties of a textured antireflective coating (ARC) polymeric film are engineered by combining the down-conversion effect of large phosphor particles and the multiple scattering effect of SiO_2 nanoparticles. In order to address the parasitic absorption of ultraviolet (UV) light, phosphors are added to convert UV light to visible light. However, the embedded phosphors increase the reflectance of the ARC film, due to the large particle size ($>5 \mu\text{m}$) and high refractive index ($n \approx 1.9$) of phosphors. Such a backward scattering problem of phosphors is compensated by adding spherical SiO_2 nanoparticles. Experimental and computational results show that SiO_2 nanoparticles in the ARC film decrease the reflectance by increasing the diffuse transmittance. This optically engineered ARC film successfully promotes the light absorption of the perovskite/silicon tandem solar cell, leading to the improvement of power conversion efficiency of the tandem cell from 22.48% to 23.50%.

1. Introduction

Multijunction solar cells may achieve power conversion efficiencies (PCE) that exceed that of single-junction solar cells. Out of several multijunction solar cells, perovskite/silicon (Si) tandem solar cells recently have attracted a significant amount of scientific and technological interest due to their economic advantages: materials and processes are cheap enough to be commercialized. Therefore, high-efficiency perovskite/Si tandem solar cells have been intensively studied. The record PCE of the perovskite/Si tandem solar cell has increased to

29.8% and is expected to pass 30% in near future.^[1] This fast progress has been accomplished mainly by improving materials for each functional layer of solar cells.^[2]

A design of the effective optical path of the tandem cell is another important,^[3] but relatively neglected method to promote light-electricity conversion. The purpose of this optical design is to minimize reflection losses of light particularly in the visible region and to reduce parasitic absorption of light particularly in UV region.^[4] When light is incident on the top perovskite cell of the tandem structure, $\approx 18.4\%$ of incident light is lost by reflection of the air–perovskite cell interface due to the refractive index difference ($n_{\text{air}} \approx 1$

and $n_{\text{perovskite}} \approx 2.5$).^[5] In order to reduce the surface reflection loss, fluoride material (e.g., MgF_2 , LiF) with a refractive index ($n_{\text{Magnesium fluoride}} \approx 1.41$ and $n_{\text{Lithium fluoride}} \approx 1.39$) between the air and the top transparent conductive oxide (TCO) layer is coated on the surface of the TCO as an antireflection film.^[6] However, the effect of the flat antireflection film is limited and the surface reflection still exists. To further reduce the surface reflection, textured poly (dimethylsiloxane) (PDMS) ($n_{\text{PDMS}} \approx 1.39$) films are often placed on the top of TCO.^[7] An issue of the textured PDMS film is that it exploits only multiple internal scattering and the refractive index of PDMS is not in between air and TCO.^[8] This clearly motivates further research to modify the refractive index of the textured film.

In addition to surface reflectance losses, parasitic absorption in the wavelength range of 300–1200 nm is an issue in tandem cells. In particular, parasitic absorption of the short-wavelength light ($\lambda < 500 \text{ nm}$) by the TCO^[9] and a buffer layer greatly limits UV-light absorption of the perovskite layer^[10] thereby lowering the PCE of the tandem device. Although alternative transparent electrodes such as graphene and reduced graphene oxide have been explored to increase the transmittance in the UV region,^[11] they do not fully resolve the problem. Besides, if UV light transmits to the perovskite layer, high-energy UV photons accelerate the dissociation of the perovskite layer to PbI_2 and byproducts, which can lead to rapid degradation in PCE.^[12]

To address these major problems of the optical design, the textured antireflection layer should have low surface reflection and convert potentially degrading UV light to useful visible

S. Lee, S. Bae, Y. Liu, Z. Zhou, J.-K. Lee
 Department of Mechanical Engineering and Material Science
 University of Pittsburgh
 Pittsburgh, PA 15261, USA
 E-mail: jul37@pitt.edu

C. U. Kim, Y. I. Noh, K. J. Choi
 Department of Material Science and Engineering
 Ulsan National Institute of Science and Technology (UNIST)
 Ulsan 44919, Republic of Korea
 E-mail: choi@unist.ac.kr

P. W. Leu
 Department of Industrial Engineering
 University of Pittsburgh
 Pittsburgh, PA 15261, USA

 The ORCID identification number(s) for the author(s) of this article can be found under <https://doi.org/10.1002/adfm.202204328>.

DOI: [10.1002/adfm.202204328](https://doi.org/10.1002/adfm.202204328)

light. This will boost the PCE of the device and enhance the device stability under UV light. UV-down-conversion ability of $\text{Yb}^{3+}/\text{Ce}^{3+}$ co-doped $\text{CsPbCl}_{1.5}\text{Br}_{1.5}$ quantum dots (QDs) and Mn^{2+} doped CsPbCl_3 QDs have been investigated to meet this complex.^[13] Large Stoke shift of UV light by perovskite QDs improves the photon–electron conversion of Si solar cells in UV region. However, these perovskite-based QDs have relatively high refractive index (>2.5) and increase the surface reflection.^[14] $\text{YVO}_4:\text{Bi}^{3+}/\text{Eu}^{3+}$ nanophosphors, Mn^{2+} doped $\text{Cd}_x\text{Zn}_{1-x}\text{S}/\text{ZnS}$ QDs, and $\text{CuGaS}_2/\text{ZnS}$ nanocrystals have been also tested to change UV light to visible light on the front side of Si solar cells.^[15] While they increase the PCE of Si solar cells initially, the exposure of QDs to oxygen, water, and thermal heating degrades the down-conversion performance of the devices.^[16] Organic UV dyes of rare-earth complexes are another material choice that can down-convert UV light.^[17] In spite of their good optical performance, the widespread use of the organic dyes in solar cells is hindered by their high cost. Cheap and stable silicate-based phosphors such as $(\text{Ba}, \text{Sr})_2\text{SiO}_4:\text{Eu}^{2+}$ phosphors can promote the perovskite/Si tandem solar cells in UV range.^[18] Still, the problem of these silicate phosphors is that their large particle size (>5 μm) is too large to suppress the backward scattering (i.e., diffuse reflectance) of the incident light.^[19]

In this work, $(\text{Ba}, \text{Ca}, \text{Eu}, \text{Sr})_2\text{SiO}_4$ (silicate-based green phosphors are denoted as SGA) phosphors of 3–10 μm in diameter and SiO_2 nanoparticles of 100 nm in diameter are embedded in the textured PDMS to convert UV light and increase the diffuse transmittance of the incident light. A mixture of SGA phosphors and SiO_2 nanoparticles considerably reduces the reflectance while suppressing the parasitic absorption of UV light. This is because the down conversion by SGA particles decreases the UV absorption and multiple scattering of embedded nanoparticles maximizes forward scattering power. Therefore, the PDMS–nanoparticle composite of a textured shape successfully improves the performance of the perovskite/Si tandem solar cell. In comparison to a pure PDMS texture film, the textured PDMS–phosphor– SiO_2 nanoparticle composite increases the PCE of the perovskite/Si tandem cell from 22.48% to 23.50%.

2. Results and Discussion

To control the reflectance of visible light and the parasitic absorption of UV light, we embedded SGA phosphors and SiO_2 nanoparticles into the textured PDMS film that is used as an antireflective coating (ARC) film on the device composed of a monolithic perovskite/Si tandem solar cell. Commercially available SGA phosphors are selected as a luminophore to provide UV-down conversion function to the ARC film. The schematic of the ARC film embedded with SGA phosphors and SiO_2 nanoparticles and the tandem solar cell with the ARC film is shown in Figure 1a,c. PDMS, which is a highly versatile material used in different research fields, is fabricated to a textured film. Figure S1 (Supporting Information) shows scanning electron microscope (SEM) images of textured Si that can be replicated on the surface of PDMS film. The micro pyramid texture shape is designed to be 3–5 μm in width and in height. Large SGA phosphors and small SiO_2 nanoparticles are mixed in the PDMS film that is attached to the IZO film. Figure 1b shows

photographs of the ARC film in ambient light and under UV light ($\lambda = 365$ nm). Strong yellow-green light emission under UV light indicates that the phosphors are uniformly distributed in the ARC film. Figure 1d indicates cross-sectional SEM image of the perovskite/Si tandem cell. The top perovskite solar cell has a typical stack composed of poly[bis(4-phenyl)(2,4,6-trimethylphenyl)amine] (PTAA)/mixed perovskite/[6,6]-Phenyl-C61-butyric acid methyl ester (PC₆₁BM)/ZnO/indium zinc oxide (IZO). In the top cell, the PC₆₁BM/ZnO layers are used as the electron selective layer and the IZO layer with 100 nm thickness is a transparent conductive electrode for the top illumination. The mixed halide perovskite layer $(\text{Cs}_{0.05}\text{FA}_{0.75}\text{MA}_{0.20})\text{Pb}(\text{I}_{0.75}\text{Br}_{0.25})_3$ absorbs most of the visible light. The bottom cell is a p-type Si solar cell with an aluminum back-surface field (BSF) layer and converts near IR light to electricity. For the optimal current matching between the top and bottom cells, the thickness of the perovskite layer is controlled to be 340 nm.^[20] Although the PC₆₁BM/ZnO/IZO layers provide transparency for the top illumination, there is a current density (mA cm^{-2}) loss of 1.08 due to the parasitic absorption in the UV region as shown in Figure S2 (Supporting Information). The effect becomes significant below 380 nm wavelength. Thus, this device structure is designed to minimize the loss of the UV light by the parasitic absorption of PC₆₁BM/ZnO/IZO and maximize the diffuse transmittance.

Figure 2a shows PL excitation (black curve) and PL emission (red curve) spectra of the SGA phosphors. SEM images of the SGA phosphors in the inset of Figure 2a indicate that the particle size is between 3 and 8 μm . SGA phosphors absorb light in the range of 280–470 nm, and the peak absorption is found at 380 nm, which is overlapped with the parasitic light absorption spectrum of the perovskite/Si tandem solar cell. Emission of SGA occurs in the range of 450–660 nm, which can be harnessed by the perovskite layer. Thus, this commercial phosphor serves as the down-conversion material for the perovskite/Si tandem solar cell. To systematically investigate an effect of the phosphors on optical property of ARC film, we fabricated a series of composite films having only SGA phosphors with five different volume concentrations (0%, 0.4%, 0.8%, 1.2%, and 1.6%). The corresponding film is denoted as ARC, ARC_SGA(0.4), ARC_SGA(0.8), ARC_SGA(1.2), and ARC_SGA(1.6), respectively. Figure 2b–d shows total transmittance, diffuse transmittance, and reflectance of the ARC_SGA films on glass. Figure 2e,f shows the PCE and incident photon to current conversion efficiency (IPCE) of the perovskite/Si tandem solar cell device with the ARC film as a function of the volume concentration. The device without and with the ARC film exhibits J_{sc} of 14.70 and 16.02 mA cm^{-2} , V_{oc} of 1.75 and 1.75 V, and FF of 80.23% and 80.18%. This results in the improvement of PCE from 20.64 to 22.48% (Table S1, Supporting Information). The textured surface of pure PDMS film (ARC) contributes to reducing the reflectance and trapping the incident light. When ARC_SGA(0.4) is applied to the device, J_{sc} and PCE increase to 16.21 mA cm^{-2} and 22.75%, respectively. IPCE curves in Figure 2f clearly show that the addition of SGA increases IPCE in UV region by harnessing UV light that has a parasitic absorption problem. It is also noted that the small amount of SGA increases IPCE in the visible range. Though total transmittance of ARC_SGA(0.4) is slightly lower than that of ARC, ARC_SGA(0.4) slightly increases the

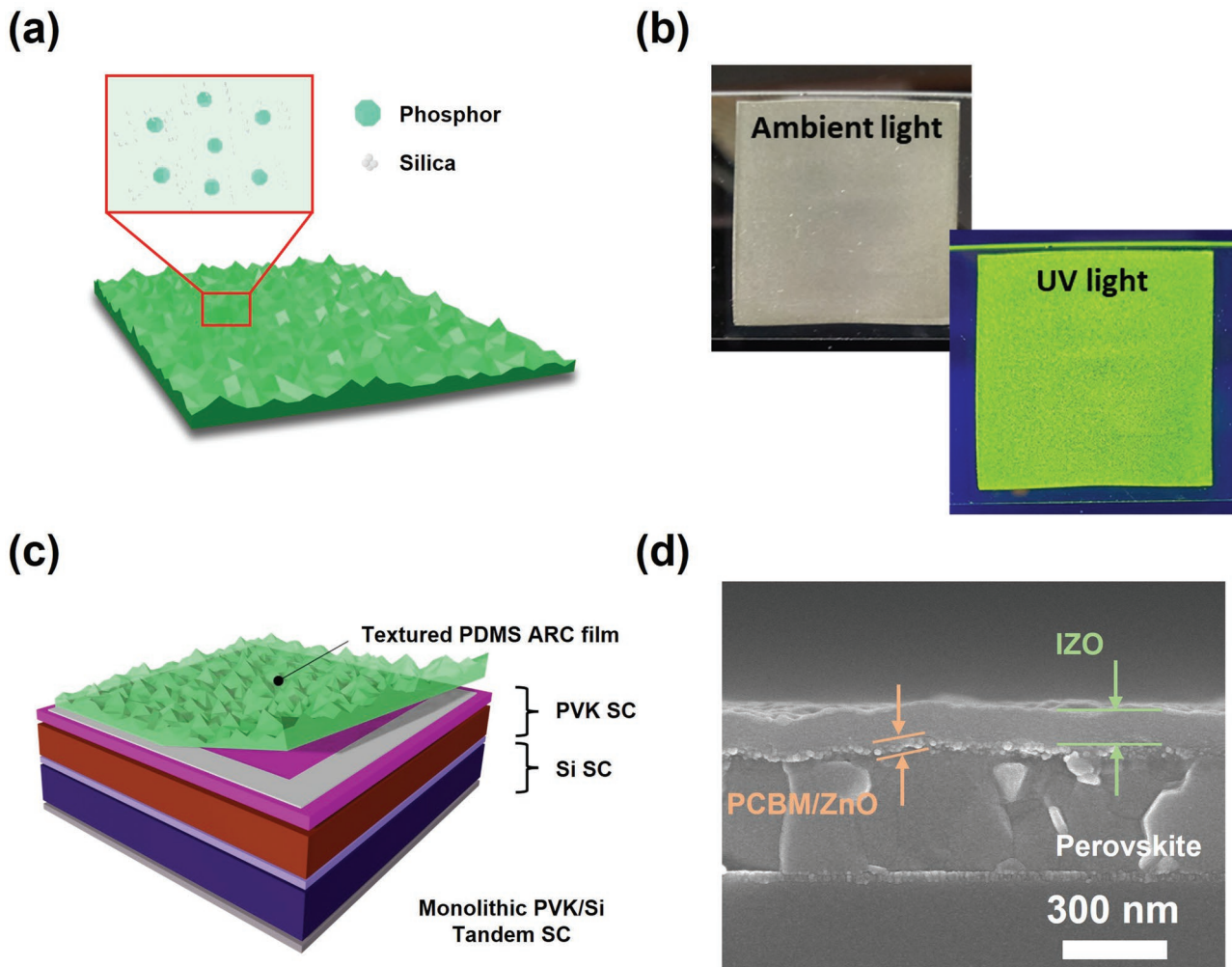


Figure 1. a) A schematic of the PDMS layer containing SGA phosphors and SiO_2 nanoparticles, b) photographs of the PDMS layer with SGA phosphors and SiO_2 nanoparticles under ambient light and UV light ($\lambda = 365 \text{ nm}$), c) a schematic of perovskite/Si tandem solar cell with the PDMS layer containing SGA phosphors and SiO_2 nanoparticles, and d) a cross-sectional SEM image of the perovskite–Si solar cell.

diffuse transmittance in the visible range and improves IPCE. However, as the volume concentration of SGA increases, the PCE of the device decreases. This is because the higher refractive index ($n \approx 1.7\text{--}1.9$)^[21] and larger size ($\approx 5 \mu\text{m}$ in diameter) of SGA decreases the total transmittance (Figure 2b). Since the size of SGA particles is larger than the wavelength of incident light, SGA also contributes to increase the backward scattering at the SGA–PDMS interface and decreasing the diffuse transmittance (Figure 2c).

Results in Figure 2 suggest that SGA can convert UV light to electricity without a parasitic absorption issue; however, it decreases the overall current of the solar cell by increasing the reflectance. For higher performance solar cells, the backward scattering of visible and near infrared (NIR) light needs to be suppressed. To address this problem, SiO_2 spherical nanoparticles with the diameter of 100 nm shown in Figure 3a are added into ARC film and their forward scattering power is explored. Due to a smaller difference in the refractive index between SiO_2 ($n \approx 1.46$) and PDMS ($n \approx 1.39$), a spherical shape and a small size, the addition of SiO_2 nanoparticles are expected to

strengthen the scattering of the incident light in forward direction without optical losses. Figure S3 (Supporting Information) shows the total transmittance of SiO_2 particles on glass as a function of size with the same volume concentration (0.8 vol.%). The total transmittance of the 30 nm-sized SiO_2 particles on glass is lower than that of glass. As the nanoparticle size increases to 100 nm, the total reflectance also increases. This is because an increase in the nanoparticle size increases the ratio of forward scattering power/backward scattering power in Mie scattering regime.^[22] However, as the particle size gets close to the wavelength of the incident light, incident light starts to be reflected. This is a case of SiO_2 particles with the diameter of 340 and 1300 nm.^[19] Due to the reflectance, the transmittance is reduced again. Therefore, SiO_2 nanoparticles with the diameter of 100 nm are chosen to increase the forward scattering of the ARC film. A textured PDMS film containing 0.8 vol.% of 100 nm SiO_2 nanoparticles is named as ARC_S(0.8).

Figure 3b–d shows the total transmittance, diffuse transmittance, and reflectance of ARC and ARC_S(0.8). In contrast to SGA, SiO_2 nanoparticles (0.8 vol.%) slightly increase the

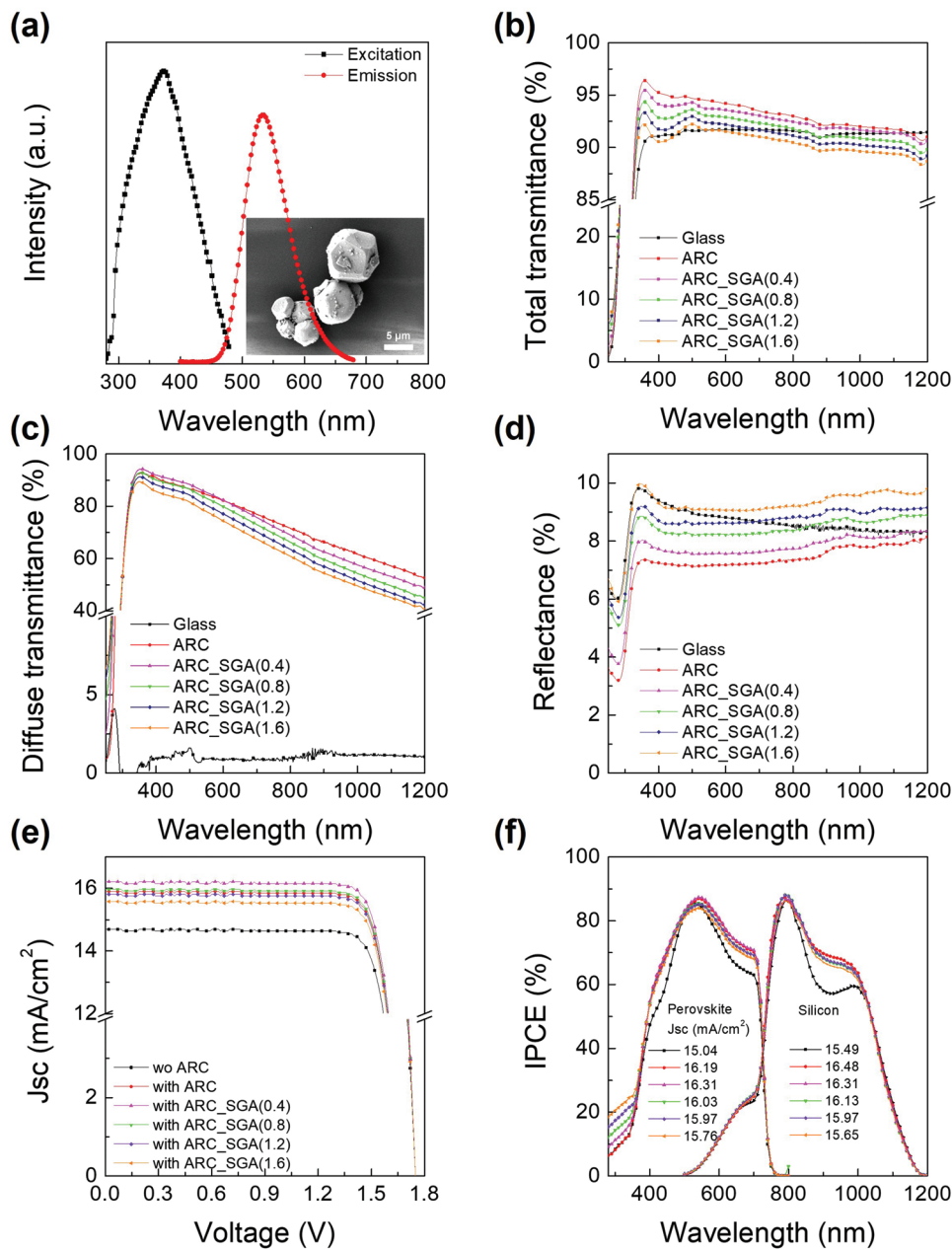


Figure 2. a) Excitation ($\lambda_{\text{ex}}: 380 \text{ nm}$) and Emission ($\lambda_{\text{em}}: 530 \text{ nm}$) of SGA phosphors. (inset: SEM image of SGA phosphors. b) total transmittance, c) diffuse transmittance, and d) reflectance of ARC film on glass with different volume % of SGA phosphors. e) J - V and f) IPCE curves of tandem solar cell with the same films.

transmittance of ARC. The total reflectance of ARC_S(0.8) is less than that of ARC, which is more pronounced in the NIR region. This is because SiO₂ nanoparticles increase the diffuse transmittance via multiple scatterings. As shown in Figure 3c, the difference in the diffuse transmittance between ARC and ARC_S(0.8) becomes more pronounced with increasing wavelength. Therefore, the reflectance of ARC_S(0.8) is lower than that of ARC (see Figure 3d). Average reflectance in UV, vis, and NIR regimes is 5.6% for ARC and 4.4% for ARC_S(0.8). Electric current obtained by integrating the reflectance (i.e., reflection loss) decreases from 2.48 (ARC) to 1.92 mA cm⁻² (ARC_S(0.8)).

Figure 3e shows the effect of ARC and ARC_S(0.8) on the performance of perovskite/Si tandem solar cells. In comparison to the PCE of a control sample without ARC (20.64%), the PCE of the device with ARC and ARC_S(0.8) is 22.48% and 23.26%, respectively. This is due to the increase in J_{sc} of 0.56 mA cm⁻². Figure 3f indicates that the addition of 100 nm SiO₂ nanoparticles increases IPCE in the entire range and the improvement becomes more conspicuous in the NIR region where the diffuse transmittance accounts for >90% of total transmittance. This suggests that a decrease in the reflectance and an increase in the effective thickness of the light absorber (a perovskite

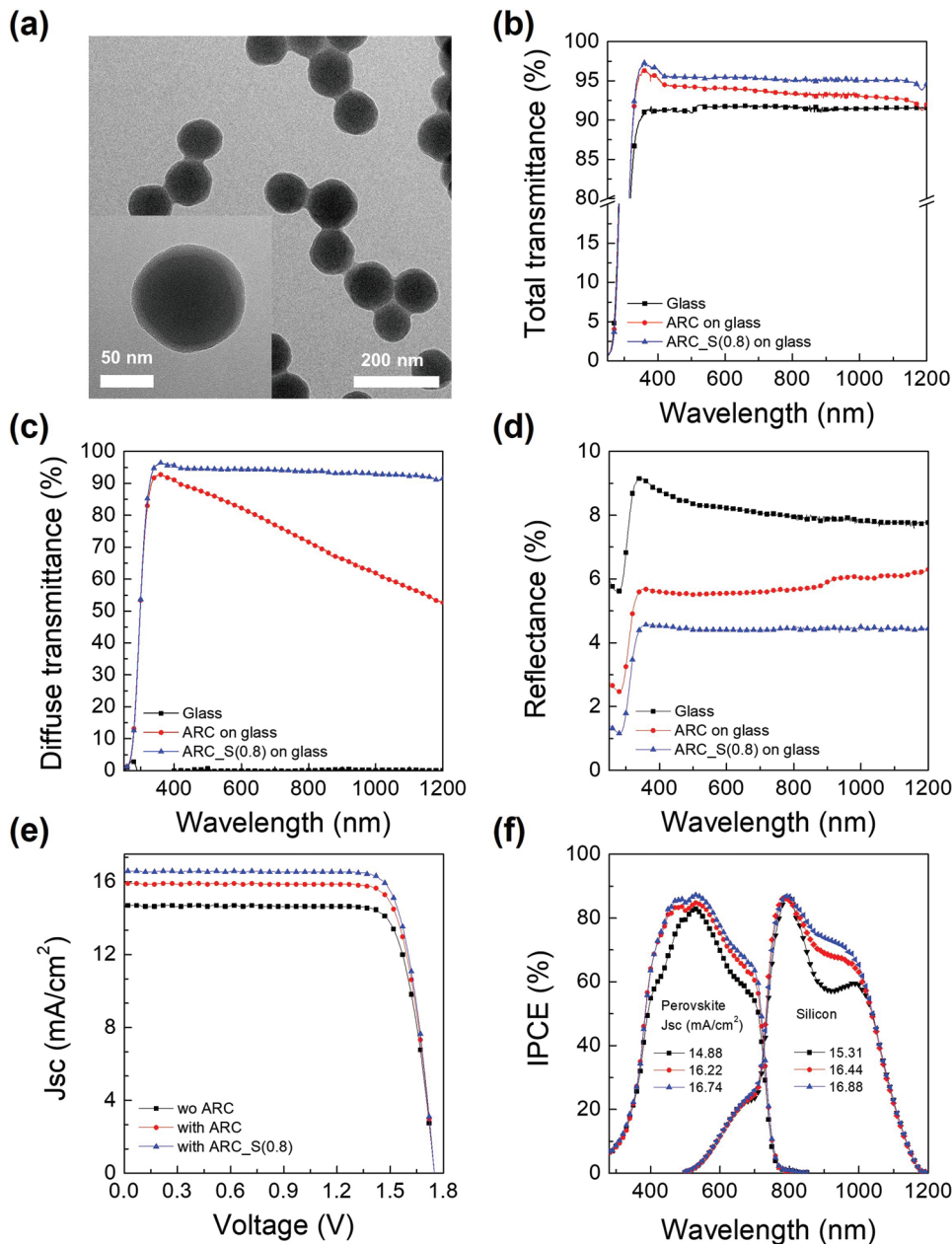


Figure 3. a) SEM image of SiO_2 nanoparticles. b) Total transmittance, c) diffuse transmittance and d) reflectance of Glass, textured ARC film on glass, and textured ARC_S (0.8) on glass. e) J - V curves and f) IPCE of tandem soar cell without and with the same films.

layer and a Si layer) promote the conversion of incident photons to electricity.

To better understand the observed diffuse scattering in Figure 3c, 3D finite-difference time domain (FDTD) simulations on the scattering effect are conducted and the diffuse transmittance is separated from the specular transmittance. Two models are used to estimate the effect of multiple scattering on the diffuse transmittance of red and near-IR light. Schematics of these two models are shown in Figure 4a. For a single scattering model, a 100 nm size spherical SiO_2 particle is added as a scatter in the PDMS matrix. The refractive index of PDMS and SiO_2 is 1.39 and 1.46 at 623 nm, respectively, and

the extinction coefficients are negligible for the simulated wavelength region. It is assumed that the SiO_2 interfaces are not perfect, because the observed scattering effect is significantly larger than the calculated one using a refractive index difference between PDMS and SiO_2 . Therefore, on the assumption that the PDMS – SiO_2 interface is not perfectly matched, a thin air-gap with a thickness of 10 nm is added between PDMS and SiO_2 . For the multiple scattering model, the system is stretched nine times along x , y , and z directions, and 729 SiO_2 @Air particles are randomly distributed in the PDMS with the same ratio, 0.8 vol.%. Figure 4b shows the scattering cross-sections that are calculated by normalizing the scattered power to the

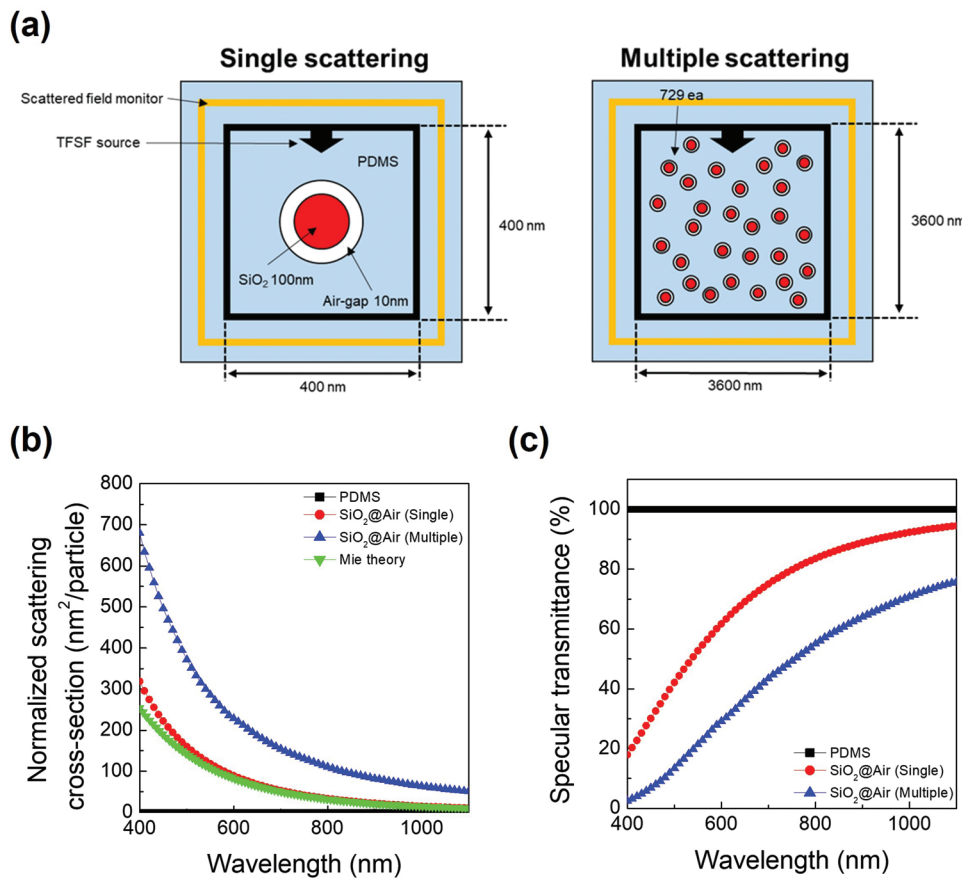


Figure 4. a) Schematic of the FDTD simulation setup for the single-particle (SiO_2 @Air) scattering model and the multiple scattering model. For the single scattering model, a 100 nm size SiO_2 particle with a 10 nm air-gap (SiO_2 @Air) is added as a scatter in the PDMS matrix (0.8 vol.-%). For the multiple scattering model, 729 SiO_2 @Air particles are randomly distributed in the PDMS with the same volume %. The refractive index of PDMS and SiO_2 is 1.39 and 1.46 at 623 nm, respectively. b) Normalized scattering cross-section for PDMS only, single scattering of SiO_2 @Air, and multiple scattering of SiO_2 @Air systems. c) Estimated specular transmittance for 150 μm thick films based on the scattering cross-section results. Air/PDMS and PDMS/substrate interface conditions were not considered.

source intensity. Note that the normalized cross-section of the multiple scattering is obtained by dividing the calculation value by a number of particles (729) involved in the simulation. This allows for comparing the actual multiple scatterer's effect compared to the single scatterer's effect. As shown in Figure 4b, the calculated single scatterer's effect is in a good agreement with the prediction of Mie scattering theory. As a number of scatterers increases, the scattering cross-section increases dramatically, which is more pronounced in the long wavelength range. A relative increment is 113% increase at $\lambda = 400$ nm, 213% increase at $\lambda = 750$ nm, and 319% increase at $\lambda = 1100$ nm. As a result, the specular transmittance of the multiple scattering system becomes significantly smaller than that of the single scattering system in red and NIR regions.^[23] Figure 4c shows that the specular transmittance decreases from $\approx 100\%$ (only PDMS) to $\approx 70\%$ (PDMS + SiO_2 NPs) for red and near-IR light when the multiple scattering is considered in a simulation process. A 30% decrease of the specular transmittance by embedded SiO_2 NPs explains well the experimentally observed diffuse transmittance in Figure 3c.

To combine the down-conversion effect and the increased forward scattering, SGA particles and 100 nm SiO_2 nanoparticles

are added into the ARC film together. Figure 5a,b shows the total transmittance and diffuse transmittance of ARC films containing both SGA phosphors and SiO_2 nanoparticles. Four different volume concentrations of SGA (0.4, 0.8, 1.2, and 1.6 vol.-%) are chosen and named as ARC_S(0.8)SGA(0.4), ARC_S(0.8)SGA(0.8), ARC_S(0.8)SGA(1.2), and ARC_S(0.8)SGA(1.6). Comparison of Figure 2 and Figure 5 reveals that the addition of SiO_2 NPs into ARC_SGA increases both total transmittance and diffusion transmittance. This is consistent with the simulation results in Figure 4 showing the enhanced diffuse transmittance by SiO_2 NPs. The multiple scattering of incident light by SiO_2 NPs suppresses the reflectance and increases the diffuse transmittance. In comparison to ARC, ARC_S(0.8)SGA(0.8) exhibits much larger diffuse transmittance in the NIR region and similar reflectance in the visible region in Figure 5b and Figure S4 (Supporting Information). Detailed numbers for total transmittance, diffuse transmittance, and reflectance of the ARC films at longer wavelength (1000 nm) are summarized in Table S2 (Supporting Information). This suggests that SiO_2 NPs can compensate for the backward scattering of large SGA particles. Figure 5c,d shows J-V curves and IPCE of the tandem solar cells with different antireflection films. The perovskite/Si

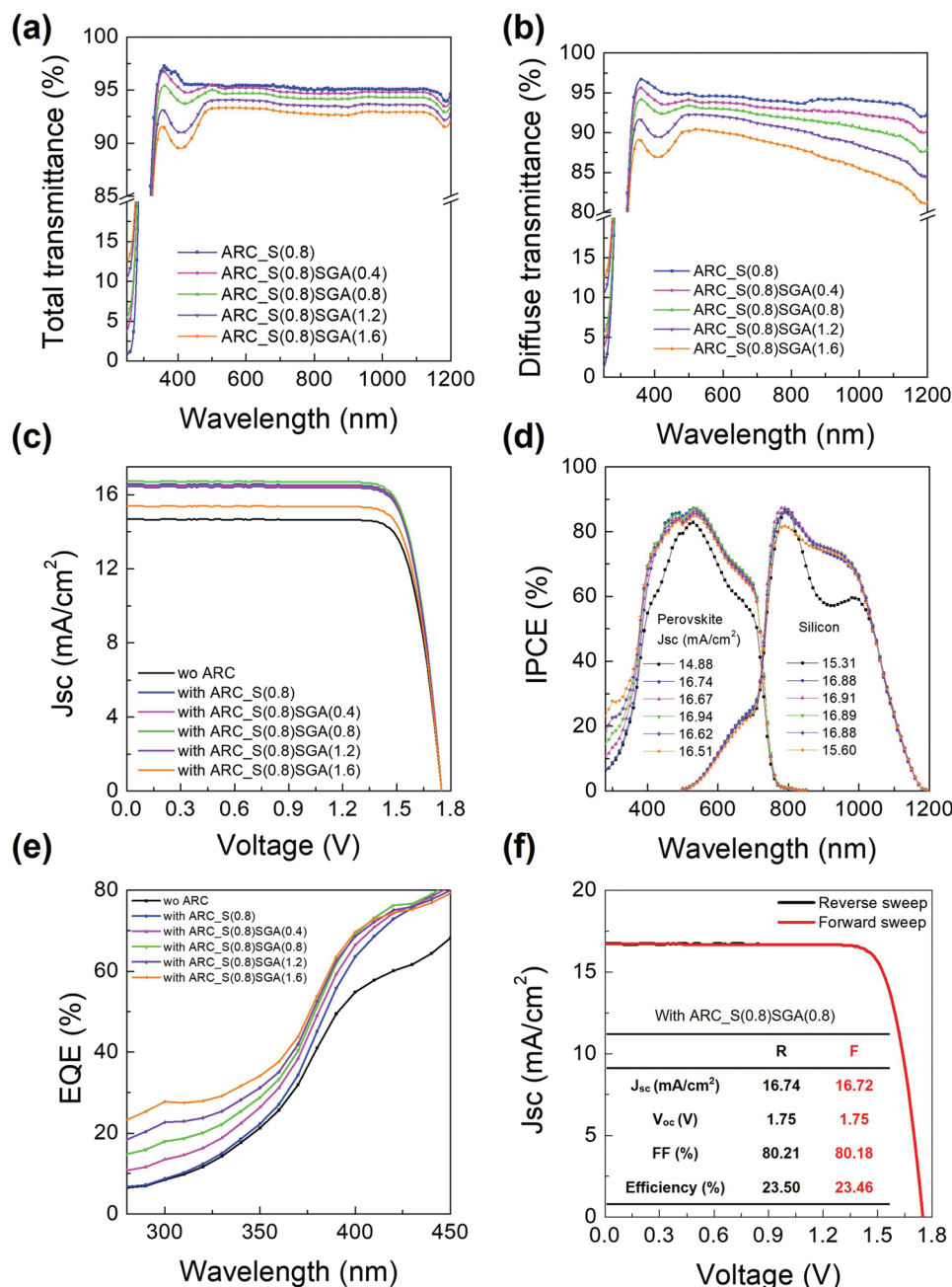


Figure 5. a) Total transmittance and b) diffuse transmittance of ARC_S(0.8) with different volume % (0.4, 0.8, 1.2, 1.6%) of SGA phosphors (ARC_S(0.8), ARC_S(0.8)SGA(0.4), ARC_S(0.8)SGA(0.8), ARC_S(0.8)SGA(1.2), and ARC_S(0.8)SGA(1.6)), c) J-V curves and d) IPCE of the tandem solar cell without and the antireflection films of SGA and SiO₂ nanoparticles, e) the magnified IPCE spectrum below 450 nm, and f) hysteresis of the tandem solar cell with ARC_S(0.8)SGA(0.8).

tandem solar cell with ARC_S(0.8)SGA(0.8) film exhibits J_{sc} of 16.74 mA cm⁻², V_{oc} of 1.75 V, and FF of 80.21% with no hysteresis in Figure 5f. The PCE was determined using maximum power point tracking (MPPT) information in Figure S5 (Supporting Information). PCE of the tandem solar cell with ARC_S(0.8)SGA(0.8) is 23.50% while PCE of the tandem solar cell with ARC_S(0.8) is 23.26%. This change in PCE is because the down-conversion of UV light ($280 \text{ nm} < \lambda < 430 \text{ nm}$) by SGA increases J_{sc} (Figure 5e). In addition, UV stability can

be enhanced by the ARC film with the incorporation of phosphors. To clearly see the UV stability effect on the solar cell performance, a perovskite solar cell with a structure of Au/Spiro-OMeTAD/Perovskite/TiO₂/FTO was used. UV stability of the device was improved under UV (365 nm) irradiation at the dosage of 15 W cm⁻² as shown in Figure S6 (Supporting Information) due to the UV down conversion effect of phosphors. The PCE of the device with the ARC film was sustained for 120 h, maintaining 91% of its initial value. The effect of

SGA phosphor on the improvement of IPCE in the UV region is clearly observed in Figure 5d. However, when the SGA concentration is >0.8 vol.%, a loss in J_{SC} by the increased reflectance cancels a gain in J_{SC} by the down-conversion effect.

3. Conclusion

We systematically demonstrate that a combination of SiO_2 nanoparticles and large phosphor particles can convert UV to visible light and increase total transmittance of ARC film. Large phosphor particles that are embedded in PDMS-ARC cause the down-conversion of UV light and increase the diffuse reflectance. Addition of a small amount of SiO_2 nanoparticles compensates for the backward scattering of large phosphor particles through a multiple scattering, leading to the improved diffuse transmittance particularly at longer wavelength (red and NIR region). This optical engineering of PDMS-ARC by embedded particles increases the PCE of the perovskite/Si tandem solar cells from 22.48% to 23.50%. Such an improvement in PCE is mainly attributed to an increase in J_{SC} that results from the suppressed reflectance and down-conversion of UV light. This work shows how to engineer ARC to improve the optical performance of the tandem solar cell.

4. Experimental Section

Fabrication of a Textured Si Mold: Si substrate was first cut into square pieces, 30 mm × 30 mm, and cleaned with acetone, deionized (DI) water, and ethanol using ultrasonification for 10 min, respectively. Before wet etching, the Si substrate was immersed in a buffered oxide etchant (BOE) in order to remove the native oxide layer on the surface of Si substrate. After that, the Si sample was subsequently rinsed with DI water and dried using N_2 gas flow. To fabricate micro-pyramidal Si mold, the Si substrate was chemically wet etched by dipping into a potassium hydroxide solution at 95 °C for 10 min and a mixed solution with KOH, IPA, and DI water (8:5:100 v/v) at 70 °C for 40 min. The sample was rinsed with DI water and dried with N_2 gas.

Synthesis of SiO_2 Particles: 30 nm SiO_2 NPs were purchased from US Research Nanomaterials, Inc. 100, 340, and 1300 nm SiO_2 NPs were synthesized by a Stöber method. A homogeneous solution was prepared by mixing NH_4OH (3 mL for 100 nm and 4.5 mL for 340 nm) and ethanol (50 mL) with magnetic stirring (500 rpm) at room temperature overnight. TEOS (1.5 mL of Tetraethyl orthosilicate) was dropped by drop into the solution while stirring. The solution was continued to stir for 12 h to form a transparent silica sol. The silica particles were collected by centrifugation at 8000 rpm for 20 min and then redispersed in ethanol for three times. For 1300 nm, a seed solution (500 nm SiO_2) was prepared by addition of TEOS (3.9 mL) slowly to a solution of NH_4OH (10.75 mL) and ethanol (50 mL). After that, the seed solution was mixed with NH_4OH (11.8 mL), ethanol (50 mL) and TEOS (4.2 mL) to form 1300 nm SiO_2 NPs. The solution was kept at room temperature with magnetic stirring (500 rpm) for 24 h. Figure S7 (Supporting Information) shows TEM and SEM images of SiO_2 nanoparticles.

Fabrication of Antireflective Coating Films: Silicate-based green phosphors (SGA 550 100 isiphor) were purchased from Merck KgaA, Darmstadt, Germany. To prevent agglomeration of phosphors, the powder was first dispersed in ethanol using sonification and added into the PDMS solution with the volume percent of 0.0%, 0.4%, 0.8%, 1.2%, and 1.6%. A PDMS solution was prepared by using a mixture of base resin and curing agent (10:1 wt.%) (Sylgard 184, Dow Corning Co.). After fully removing the ethanol by vacuum for 2 h, SiO_2 particles were added into the solution and mixed carefully. The PDMS solution with the

mixture of phosphors and SiO_2 particles poured on the textured Si mold and cured at 65 °C overnight. The film was transferred to the top surface of the perovskite/Si tandem solar cell.

Fabrication of Si Solar Cell: Si wafer (monocrystalline Si wafers (1–5 Ω cm, p-type, CZ, 525 μm) was cleaned using the RCA cleaning procedure. Two micro meter thick aluminum was deposited on the back side of the Si wafer using an e-beam evaporator. Spin on dopant (Filmtronics SOD P507) was coated on the front side of the Si wafer using spin coating. The doping level was controlled and optimized using a rapid thermal annealing (RTA) system. An emitter with a sheet resistance of 100 ohms sq^{-1} was made on the front side, and P + Al BSF was made on the back side. The remaining phosphorous silicate glass was oxidized using an RTA system and removed with hydrofluoric acid. After that, 1 μm Ag metal electrode was deposited on the back side using this beam. Finally, 20 nm thick ITO was deposited through an RF magnetron sputtering process to form a recombination layer.

Fabrication of Perovskite Solar Cell and Tandem Solar Cell: PTAA solution (2 mg mL^{-1} in chlorobenzene) was spin-coated on the substrates at 6000 rpm for 30 s and annealed at 100 °C for 10 min. A 0.5 mg mL^{-1} PFN-Br solution in methanol was spin-coated on the PTAA HEL at 5000 rpm for 30 s. For preparing the $\text{Cs}_{0.05}(\text{FA}_{0.83}\text{MA}_{0.17})_{0.95}\text{Pb}(\text{I}_{0.75}\text{Br}_{0.25})_3$ mixed perovskite solution, 1.35 M FAPbI_3 with 10% excess PbI_2 and 1.35 M MAPbBr_3 in a N, N-dimethylformamide (DMF)/dimethyl sulfoxide (DMSO) (4:1 v/v) cosolvent and 1.5 M CsI stock solution in DMSO were prepared separately. Then the FAPbI_3 , MAPbBr_3 and CsI solutions were mixed in a 750:250:53.7 volume ratio. The mixed perovskite solution was cast by an anti-solvent dropping method. The spin-coating consists of spinning at 5000 rpm for 1.7 s for ramping time and at 5000 rpm for 30 s for the keeping step. After 10 s, the spinning substrate was washed with 300 μL ethyl acetate as an anti-solvent. Then, perovskite films were annealed at 100 °C for 1 h. The PCBM (OSM) solution (20 mg mL^{-1} in chlorobenzene) was spin-coated at 4000 rpm for 30 s, and the ZnO solution (Avantama) was also heat treated at 100 °C for 1 min after coating under the same conditions. Then, 100 nm thick Ag electrodes were deposited using an e-beam evaporator. The monolithic perovskite/Si tandem solar cell was fabricated by applying the semitransparent perovskite solar cell process on top of the tandem-oriented bottom Si solar cell. The device area, which was defined by shadow mask, was 0.25 cm^2 .

Characterization: The J - V characteristics of the perovskite/Si tandem solar cells were measured under AM 1.5 G (100 mW cm^{-2}) conditions with illumination with aperture mask (0.25 cm^2). The IPCE spectra were measured using the QE Measurement system (Newport), by applying monochromatic lights from a Xenon lamp under ambient conditions. Total transmittance and diffuse transmittance were measured by using a UV-vis-NIR spectrophotometer with a 100 nm diameter integrating sphere (LAMBDA 750, Perkin Elmer). Photoluminescence (PL) measurement was performed using spectrofluorometer (QuantaMaster, PTI). Excitation and Emission spectra were recorded at 280–480 and 400–680 nm in 1 nm increments, respectively.

Supporting Information

Supporting Information is available from the Wiley Online Library or from the author.

Acknowledgements

S.L. and C.U.K. contributed equally to this work. This work was supported by the Korea Institute of Energy Technology Evaluation and Planning grant funded by the Korea government (202113091010010, Super Solar Cells – Development of double junction solar cells breakthrough for the theoretical limit of silicon solar cell efficiency (>35%)). J.K. Lee acknowledges the support through NSF (ECCS 1709307). K.J. Choi acknowledges the support through the National Research Foundation of

Korea grant funded by the Korea government (NRF-2018R1A2B2003720), Technology Development Program to solve climate changes of the National Research Foundation (NRF) funded by the Ministry of Science, ICT (2019M1A2A2072416), and the National Research Foundation of Korea grant funded by the Korea government (2021M3H4A1A02051234).

Conflict of Interest

The authors declare no conflict of interest.

Data Availability Statement

The data that support the findings of this study are available from the corresponding author upon reasonable request.

Keywords

antireflective coatings, phosphors, scattering, SiO₂ particles, tandem solar cells, UV down conversion

Received: April 21, 2022

Revised: May 27, 2022

Published online:

- [1] a) A. Al-Ashouri, E. Köhnen, B. Li, A. Magomedov, H. Hempel, P. Caprioglio, J. A. Márquez, A. B. M. Vilches, E. Kasparavicius, J. A. Smith, N. Phung, D. Menzel, M. Grischek, L. Kegelmann, D. Skroblin, C. Gollwitzer, T. Malinauskas, M. Jošt, G. Matič, B. Rech, R. Schlatmann, M. Topič, L. Korte, A. Abate, B. Stannowski, D. Neher, M. Stolterfoht, T. Unold, V. Getautis, S. Albrecht, *Science* **2020**, *370*, 1300; b) B. Ehrler, E. Alarcón-Lladó, S. W. Tabering, T. Veeken, E. C. Garnett, A. Polman, *ACS Energy Lett.* **2020**, *5*, 3029.
- [2] K. A. Bush, A. F. Palmstrom, Z. J. Yu, M. Boccard, R. Cheacharoen, J. P. Mailoa, D. P. McMeekin, R. L. Z. Hoye, C. D. Bailie, T. Leijtens, I. M. Peters, M. C. Minichetti, N. Rolston, R. Prasanna, S. Sofia, D. Harwood, W. Ma, F. Moghadam, H. J. Snaith, T. Buonassisi, Z. C. Holman, S. F. Bent, M. D. McGehee, *Nat. Energy* **2017**, *2*, 17009.
- [3] M. Jošt, E. Köhnen, A. B. Morales-Vilches, B. Lipovšek, K. Jäger, B. Macco, A. Al-Ashouri, J. Krč, L. Korte, B. Rech, R. Schlatmann, M. Topič, B. Stannowski, S. Albrecht, *Energy Environ. Sci.* **2018**, *11*, 3511.
- [4] E. Köhnen, M. Jošt, A. B. Morales-Vilches, P. Tockhorn, A. Al-Ashouri, B. Macco, L. Kegelmann, L. Korte, B. Rech, R. Schlatmann, B. Stannowski, S. Albrecht, *Sustain. Energy Fuels* **2019**, *3*, 1995.
- [5] D. M. Bacal, N. N. Lal, A. N. Jumabekov, Q. Hou, Y. Hu, J. Lu, A. S. R. Chesman, U. Bach, *Opt. Express* **2020**, *28*, 12650.
- [6] a) J. P. Mailoa, C. D. Bailie, E. C. Johlin, E. T. Hoke, A. J. Akey, W. H. Nguyen, M. D. McGehee, T. Buonassisi, *Appl. Phys. Lett.* **2015**, *106*, 121105; b) G. Nogay, F. Sahli, J. Werner, R. Monnard, M. Boccard, M. Despeisse, F.-J. Haug, Q. Jeangros, A. Ingenito, C. Ballif, *ACS Energy Lett.* **2019**, *4*, 844; c) Y. Li, J.-D. Lin, X. Liu, Y. Qu, F.-P. Wu, F. Liu, Z.-Q. Jiang, S. R. Forrest, *Adv. Mater.* **2018**, *30*, 1804416.
- [7] F. Hou, C. Han, O. Isabella, L. Yan, B. Shi, J. Chen, S. An, Z. Zhou, W. Huang, H. Ren, Q. Huang, G. Hou, X. Chen, Y. Li, Y. Ding, G. Wang, C. Wei, D. Zhang, M. Zeman, Y. Zhao, X. Zhang, *Nano Energy* **2019**, *56*, 234.
- [8] S. Manzoor, Z. J. Yua, A. Ali, W. Ali, K. A. Bush, A. F. Palmstrom, S. F. Bent, M. D. McGehee, Z. C. Holman, *Sol. Energy* **2017**, *173*, 59.
- [9] L. Mazzarella, M. Werth, K. Jäger, M. Jošt, L. Korte, S. Albrecht, R. Schlatmann, B. Stannowski, *Opt. Express* **2018**, *16*, 487.
- [10] a) K. Jäger, L. Korte, B. Rech, S. Albrecht, *Opt. Express* **2017**, *25*, 473; b) F. E. Subhan, A. D. Khan, A. D. Khan, N. Ullah, M. Imran, M. Norman, *RSC Adv.* **2020**, *10*, 26631.
- [11] a) F. Lang, M. A. Gluba, S. Albrecht, J. Rappich, L. Korte, B. Rech, N. H. Nickel, *J. Phys. Chem. Lett.* **2016**, *6*, 2745; b) P. You, Z. Liu, Q. Tai, S. Liu, F. Yan, *Adv. Mater.* **2016**, *27*, 3632.
- [12] S.-W. Lee, S. Kim, S. Bae, K. Cho, T. Chung, L. E. Mundt, S. Lee, S. Park, H. Park, M. C. Schubert, S. W. Glunz, Y. Ko, Y. Jun, Y. Kang, H.-S. Lee, D. Kim, *Scientific Repots* **2016**, *6*, 38150.
- [13] a) D. Zhou, D. Liu, G. Pan, X. Chen, D. Li, W. Xu, H. Song, *Adv. Mater.* **2017**, *29*, 1704149; b) Q. Wang, X. Zhang, Z. Jin, J. Zhang, Z. Gao, Y. Li, S. F. Liu, *ACS Energy Lett.* **2017**, *2*, 1479.
- [14] a) R. Padmavathy, A. Amudhavalli, R. Rajeswarapalanichamy, K. Iyakutti, Z. *Naturforsch. A* **2019**, *74*, 905; b) N.-G. Park, *Nano Converg* **2016**, *3*, 15.
- [15] a) C. K. Huang, Y. C. Chen, W. B. Hung, T. M. Chen, K. W. Sun, W.-L. Chang, *Prog Photovolt.* **2013**, *21*, 1507; b) M. Jalalah, Y.-H. Ko, F. A. Harraz, M. S. Al-Assiri, J.-G. Park, *Nano Energy* **2017**, *33*, 257; c) M. Jalalah, M. S. Al-Assiri, J.-G. Park, *Adv. Energy Mater.* **2018**, *8*, 1703418.
- [16] a) H. Moon, C. Lee, W. Lee, J. Kim, H. Chae, *Adv. Mater.* **2019**, *31*, 1804294; b) J. Ko, B. G. Jeong, J. H. Chang, J. F. Joung, S.-Y. Yoon, D. C. Lee, S. Park, J. Huh, H. Yang, W. K. Bae, S. G. Jang, J. Bang, *NPG Aisa Mater.* **2020**, *12*, 19; c) T. Davidson-Hall, H. Aziz, *ACS Appl. Mater. Interfaces* **2020**, *12*, 16782.
- [17] a) F. Bella, G. Griffini, J.-P. Correa-Baena, G. Saracco, M. Grätzel, A. Hagfeldt, S. Turri, C. Gerbaldi, *Science* **2016**, *354*, 203; b) A. Gavriluta, T. Fix, A. Nonat, A. Slaoui, J.-F. Guillemoles, L. J. Charbonnière, *J. Mater. Chem. A* **2017**, *5*, 14031.
- [18] J. Zheng, H. Mehrvarz, C. Liao, J. Bing, X. Cui, Y. Li, V. R. Gonçales, C. F. J. Lau, D. S. Lee, Y. Li, M. Zhang, J. Kim, Y. Cho, L. G. Caro, S. Tang, C. Chen, S. Huang, A. W. Y. Ho-Baillie, *ACS Energy Lett.* **2019**, *4*, 2623.
- [19] K. Hou, C. Wang, X. Liu, *Int. J. Opt. Photon.* **2020**, *10*, 79.
- [20] C. U. Kim, J. C. Yu, E. D. Jung, I. Y. Choi, W. Park, H. Lee, I. Kim, D.-K. Lee, K. K. Hong, M. H. Song, K. J. Choi, *Nano Energy* **2019**, *60*, 213.
- [21] a) A. Solodovnyk, D. Riedel, B. Lipovšek, A. Osvet, J. Gast, E. Stern, K. Forberich, M. Batentschuk, J. Krč, M. Topič, C. J. Brabec, *Opt. Mater. Express* **2017**, *7*, 2946; b) M. Mikami, *ECS J. Solid State Sci. Technol.* **2013**, *2*, R3048.
- [22] a) Y. H. Fu, A. I. Kuznetsov, A. E. Mirochnichenko, Y. F. Yu, B. Luk'yanchuk, *Nat. Commun.* **2013**, *4*, 1527; b) J. R. Nagel, M. A. Scarpulla, *Opt. Express* **2010**, *18*, 139.
- [23] a) L. E. McNeil, R. H. French, *Acta Mater.* **2000**, *48*, 4571; b) W. Suthabanditpong, M. Tani, C. Takai, M. Fuji, R. Buntem, T. Shirai, *Adv. Powder Technol.* **2016**, *27*, 454.